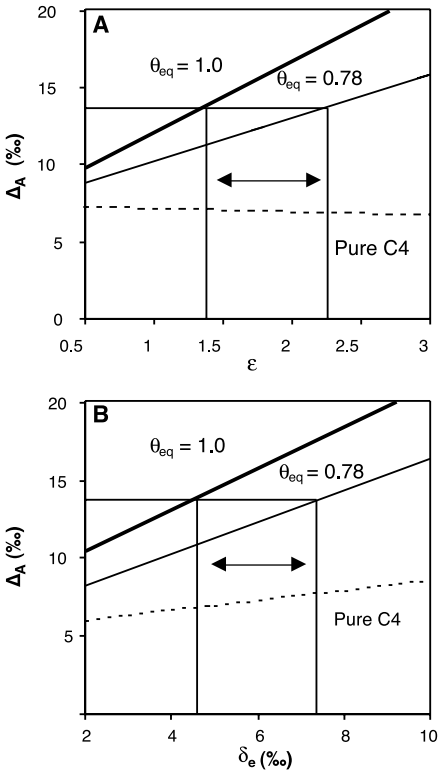

Fig. 3. Global discrimination against $C^{18}OO$, Δ_A, as a function of (**A**) ε values and (**B**) leaf-water $\delta^{18}O$ values. Discrimination is calculated from Eq. 3 with parameters given in (*6*) [δ_e = 4.8‰ in (A); $\bar{a}$ = 7.4‰, ε = 1.32 in (B); +0.4‰ is included in δ_e to allow for ^{18}O fractionation between leaf water and leaf CO_2]. The sloping lines indicate the relationships for global vegetation with (light solid line) or without (heavy solid line) the disequilibrium effect used in the global ^{18}O budget of (*6*). Also shown for comparison is the high sensitivity of global mean Δ_A to the contribution of C_4 plant productivity (dashed line, ε = 0.64). The horizontal line indicates global discrimination solved from the global mass balance of $C^{18}OO$ from (*6*). Vertical lines show how a shift in θ_{eq} from 1.0 to 0.78 can be compensated for by leaf water (realistically) or ε (unrealistically), while constrained to a constant Δ_A.

References and Notes

1. R. J. Francey *et al.*, *Nature* **373**, 326 (1995).
2. C. D. Keeling, T. P. Whorf, M. Wahlen, J. van der Plicht, *Nature* **375**, 666 (1995).
3. P. Ciais, P. P. Tans, M. Trolier, J. W. C. White, R. J. Francey, *Science* **269**, 1098 (1995).
4. R. F. Keeling, S. C. Piper, M. Heimann, *Nature* **381**, 218 (1996)
5. R. J. Francey, P. P. Tans, *Nature* **327**, 495 (1987).
6. G. D. Farquhar *et al.*, *Nature* **363**, 439 (1993).
7. D. Yakir, X. F. Wang, *Nature* **380**, 515 (1996).
8. P. Ciais *et al.*, *J. Geophys. Res.* **102**, 5873 (1997).
9. G. Dongmann, *Radiat. Environ. Biophys.* **11**, 219 (1974).
10. H. Förstel, in *Proceedings* of the *3rd International Symposium on Environmental Biogeochemistry and Geomicrobiology*, W. E. Krumbein, Ed. (Ann Arbor, MI, 1978), p. 811.
11. P. P. Tans, *Tellus* **50B**, 163 (1999).
12. M. Bender, L. D. Labeyrie, D. Raynaud, C. Lorius, *Nature* **318**, 349 (1985).
13. M. Bender, T. Sowers, L. D. Labeyrie, *Global Biogeochem. Cycles* **8**, 363 (1994).
14. J. S. Gillon, D. Yakir, *Plant Physiol.* **123**, 201 (1999).
15. c_{cs} represents the CO_2 concentration at the chloroplast surface, which is the limit of CA activity and is thus assumed to represent the site of CO_2-H_2O in leaves. c_{cs} is typically a midway value between those in the liquid-air interfaces and the sites of CO_2 assimilation inside leaves (*14*).
16. Supplementary data are available on *Science* Online at www.sciencemag.org/cgi/content/full/291/5513/2584/DC1.
17. M. D. Hatch, J. N. Burnell, *Plant Physiol.* **93**, 825 (1990).
18. E. Utsoniyama, S. Muto, *Physiol. Plant.* **88**, 413 (1993).
19. A. Makino *et al.*, *Plant Physiol. 100, 1737 (1992)*
20. G. A. Mills, H. C. Urey, *J. Am. Chem. Soc.* **62**, 1019 (1940).
21. J. S. Gillon, D. Yakir, *Plant Cell Environ.* **23**, 903 (2000).
22. The gross flux of CO_2 from atmosphere to leaf, F_{al}, was determined from leaf-scale measurements of net CO_2 assimilation, A, and c_{cs}, which are related by the expression $F_{al} = A[1 + c_{cs}/(c_a - c_{cs})]$.
23. D. Yakir, J. A. Berry, L. Giles, C. B. Osmond, *Plant Cell Environ.* **17**, 73 (1994).
24. L. B. Flanagan, S. L. Phillips, J. R. Ehleringer, J. Lloyd, G. D. Farquhar, *Aust. J. Plant Physiol.* **21**, 221 (1994).
25. T. G. Williams, L. B. Flanagan, J. R. Coleman, *Plant Physiol.* **112**, 319 (1996).
26. K. G. Harwood, J. S. Gillon, H. Griffiths, M. S. J. Broadmeadow, *Plant Cell Environ.* **21**, 269 (1998).
27. X. F. Wang, D. Yakir, M. Avishai, *Global Change Biol.* **4**, 835 (1998).
28. P. Peylin *et al.*, *Tellus* **51B**, 642 (1999).
29. R. S. Defries, J. R. G. Townshend, *Int. J. Remote Sens.* **15**, 3567 (1994).
30. Groups 1 to 5, 7, and 8, as defined in the vegetation parameterization of SiB2 (*40*), all contain trees and shrubs only, which we combine into a single group with the corresponding θ_{eq} value. Group 6 (C_4 groundcover and grassland) we assume has some C_3 component and calculate θ_{eq} from a weighting of 75:25 C_4 grasses:trees to allow for the presence of trees in savanna-type habitats. Group 9 (C_3 grassland and agriculture) we assume comprises 25:50:25 for trees:C_3 grasses:C_4 grasses; the C_3 and C_4 grasses include some C_3 herbs and C_4 grass species as crops.
31. G. Hoffmann *et al.*, in preparation.
32. J. R. Ehleringer, T. E. Cerling, B. R. Helliker, *Oecologia* **112**, 285 (1997).
33. G. J. Collatz, J. A. Berry, J. S. Clark, *Oecologia* **114**, 441 (1998).
34. J. Lloyd, G. D. Farquhar, *Oecologia* **99**, 201 (1994).
35. M. Trolier, J. W. C. White, J. R. Lawrence, W. S. Broecker, *J. Geophys. Res.* **101**, 25897 (1996).
36. R. A. Houghton, *Tellus* **51B**, 298 (1999).
37. R. H. Waring, W. H. Schlesinger, *Forest Ecosystems* (Academic Press, New York, 1985).
38. R. A. Houghton, *Bioscience* **44**, 305 (1994).
39. National Oceanic and Atmospheric Administration/Institute of Arctic and Alpine Research, www.cmdl.noaa.gov/ccg (2000).
40. P. J. Sellers *et al.*, *J. Climate* **9**, 706 (1996).
41. J. Gillon and D. Yakir, data not shown [but obtained from measurement of the Michaelis constant (K_m) on four C_3 species—*Hibiscus* sp., *Sonchus* sp., *Asparagus* sp., *and Apera* sp.—by assaying CA activity over a range (3 to 24 mM) of CO_2 concentrations].

42. We are grateful to A. S. Denning and P. Peylin for SiB2 model data, X. F. Wang for physiological data, E. Negreanu for technical help, and the Jerusalem Botanic Garden for access to their collections. Supported by a fellowship from the Leverhulme Trust, UK (J.S.G.) and by grants from the Israel Science Foundation (308/96 and 695/99) and the Minerva Foundation (D.Y.).

5 October 2000; accepted 26 February 2001
Published online 8 March 2001;
10.1126/science.1056374
Include this information when citing this paper.

Ancient Geodynamics and Global-Scale Hydrology on Mars

Roger J. Phillips,[1] Maria T. Zuber,[2,3] Sean C. Solomon,[4] Matthew P. Golombek,[5] Bruce M. Jakosky,[6] W. Bruce Banerdt,[5] David E. Smith,[3] Rebecca M. E. Williams,[1] Brian M. Hynek,[1] Oded Aharonson,[2] Steven A. Hauck II[1]

Loading of the lithosphere of Mars by the Tharsis rise explains much of the global shape and long-wavelength gravity field of the planet, including a ring of negative gravity anomalies and a topographic trough around Tharsis, as well as gravity anomaly and topographic highs centered in Arabia Terra and extending northward toward Utopia. The Tharsis-induced trough and antipodal high were largely in place by the end of the Noachian Epoch and exerted control on the location and orientation of valley networks. The release of carbon dioxide and water accompanying the emplacement of ~3 × 10^8 cubic kilometers of Tharsis magmas may have sustained a warmer climate than at present, enabling the formation of ancient valley networks and fluvial landscape denudation in and adjacent to the large-scale trough.

The western hemisphere of Mars is dominated by the Tharsis rise, a broad elevated (~10 km) region extending over 30 million square kilometers. Tharsis is the locus of large-scale volcanism and pervasive fracturing that resulted from the loading of the lithosphere, or outer elastic shell, by voluminous extrusive and intrusive magmatic deposits (*1–3*). Here we use recently acquired gravity (*4*) and topography (*5*) data from the Mars Global Surveyor (MGS) spacecraft (*6*) to determine the effect of the mass load of Tharsis on the shape and gravity field of the rest of the planet. We test the hypothesis that the deformational response to the Tharsis load is responsible for the topographic trough and the heretofore unexplained ring of negative gravity anomalies (Figs. 1 and 2A) (*7*) that surround the Tharsis rise, as well as for the major gravity and topographic highs that are

antipodal to Tharsis. We examine the influence that Tharsis may have had on the timing, orientation, and location of fluvial features on the planet. Because of the enormous mass of the Tharsis load, understanding the global history of Mars requires understanding the role that Tharsis played in that history; the formation of Tharsis may have been an exceptional phenomenon in the evolution of the terrestrial planets.

To test the hypothesis that Mars displays a global deformational response to Tharsis loading, we use a spherical harmonic model (*8*) of the loading of a spherical elastic shell (*9*) and isolate the spatially variable Tharsis topography (Fig. 3A) as the only load on the planet (*10*). The degree of compensation (*11*) of the load is about 95% (*12*), an assumption that produces consistency between predicted and observed topography but overpredicts the magnitudes of the associated gravity anomalies. Because we are interested primarily in the spatial correlation of models to observed fields, rather than model amplitudes, the mismatch of predicted and observed gravity is secondary to this discussion (*13*).

The locations of the observed and modeled ring of negative gravity anomalies (Fig. 2, A and B) around Tharsis, expanded to spherical harmonic order and degree 10 (l = 10), are consistent and include several of the intermediate-wavelength features within the ring (such as relative lows to the northwest, northeast, and east, and the relative high to the south). The model also predicts a topographic trough (here termed the Tharsis trough) around Tharsis (Fig. 3C). Such a topographic depression does surround Tharsis over at least 270° of azimuth (Fig. 3A). To the east of Tharsis, this trough extends northward from the Argyre impact basin, through Chryse and Acidalia Planitiae, to the North Polar basin. To the northwest of Tharsis, Arcadia and Amazonis Planitiae comprise the depression, whereas southwest of Tharsis, the depression becomes less evident (*14*). The fact that the ring of negative gravity anomalies persists to the southwest of Tharsis indicates that more than the surface topography is required to explain the gravity data here; one possibility is that the trough has been filled with sediments that are lower in density than average crustal material.

Antipodal to Tharsis, the model predicts a topographic high (here termed the Arabia bulge) over the elevated Arabia Terra (Fig. 3D); the predicted high also extends over the Utopia basin to the north. The planetary topographic dichotomy of a northern lowland and a southern upland (*5*) is not an element of a Tharsis loading model; however, the anomalously broad western rim of the Utopia basin (Fig. 3B) may be an expression of uplift

[1]McDonnell Center for the Space Sciences and Department of Earth and Planetary Sciences, Washington University, St. Louis, MO 63130, USA. [2]Department of Earth, Atmospheric, and Planetary Sciences, Massachusetts Institute of Technology, Cambridge, MA 02139, USA. [3]Earth Sciences Directorate, NASA/Goddard Space Flight Center, Greenbelt, MD 20771, USA. [4]Department of Terrestrial Magnetism, Carnegie Institution of Washington, Washington, DC 20015, USA. [5]Jet Propulsion Laboratory, California Institute of Technology, Pasadena, CA 91109, USA. [6]Laboratory for Atmospheric and Space Physics, University of Colorado, Boulder, CO 80309, USA.

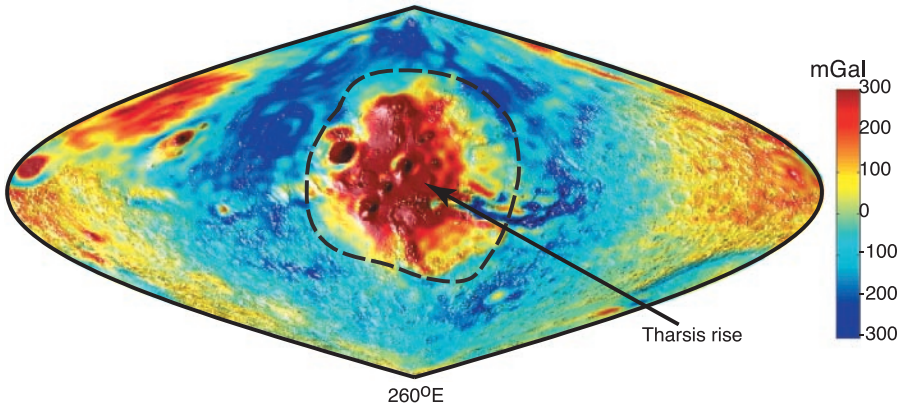

Fig. 1. Gravity anomaly image (*4*) draped over a three-dimensional (3D) view of topography (*5*) centered on Tharsis at 260°E longitude. This and all subsequent figures are in sinusoidal projection. The gravity anomaly image has been saturated at ±300 milligals (mGal) and is expanded to l = 60. The prominent topographic feature in the center is the Tharsis rise and its volcanic constructs; the approximate boundary to Tharsis is shown as a dashed line. Valles Marineris extend eastward from Tharsis. Negative portions of the gravity anomaly field form a ring around Tharsis. A region antipodal to Tharsis (seen at the right and left sides of the map near 80°E longitude) is centered on Arabia Terra, which is both a topographic and a gravitational high.

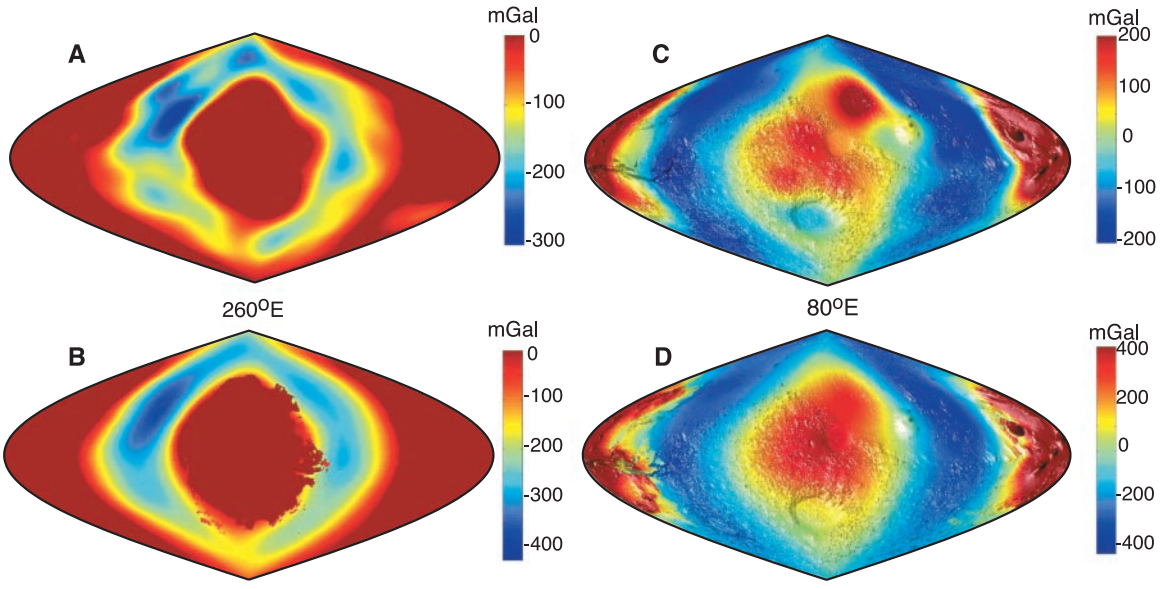

Fig. 2. (**A**) Observed and (**B**) modeled negative gravity anomaly ring around Tharsis, centered at 260°E longitude. The irregular boundary around Tharsis in the model results from defining the load boundary with a quarter-degree topographic grid (*10*). (**C**) Observed and (**D**) modeled gravity anomalies draped over a 3D view of observed topography centered on Arabia Terra at 80°E longitude. The observed gravity anomaly over Tharsis is shown in the model image. Different scales for observed and modeled fields result from an overprediction of model gravity. For (A) through (D), gravity fields are expanded to l = 10 independently inside and outside of the load boundary.

resulting from Tharsis loading. The Hellas impact basin is also outside the realm of the model, yet both the modeled and observed topography show a downward slope in Hellas rim topography (*5*) toward the South Pole. This slope, in the direction of Tharsis, suggests that a portion of the Hellas rim underwent vertical motion during the formation of the trough created by the Tharsis load. In both the observed and modeled gravity anomaly fields ($l = 10$), there is a gradient across Hellas and a high over Arabia Terra that extends northward to the Utopia basin, mirroring features in the long-wavelength topography (Fig. 2, C and D). The modeled gravity clearly does not account for the smaller scale, positive gravity anomalies at Elysium and the central Utopia basin, which reflect subsurface structures characterized, respectively, by volcanically thickened crust and a combination of crustal thinning during basin formation and infill of the basin depression (*2*). However, we conclude that the long-wavelength, nonhydrostatic gravity field of Mars is explained simply by the Tharsis load and the resulting global deformation of the lithosphere. Further, the shape of Mars is determined by these two quantities plus the northward pole-to-pole slope that formed in earliest martian history (*5*).

Extensional structures radial to the Tharsis rise and compressional structures generally concentric to the rise constitute the majority of the tectonic features in the Tharsis region (*15*). About half of these features are Noachian (*16*) in age, suggesting that tectonic activity peaked early and decreased with time (*17*). The positions and orientations of both types of structures are matched by elastic shell loading models (*18*) constrained by current gravity and topography fields (*3*). Successful models are able to predict strain levels comparable to those observed in Noachian structures (*19*) and require that the extent of the load in the Noachian be comparable to that at present. Thus, the overall Tharsis load must have been largely in place by the Late Noachian. Because they are the direct response to the Tharsis load, the Tharsis trough and Arabia bulge must also have existed since Noachian time.

The development of the Tharsis trough and Arabia bulge thus should have influenced the location and orientation of martian valley networks and outflow channels. Valley networks are the most common drainage systems on Mars (*20*). Their similarity to terrestrial river systems suggests that the genesis of valley networks involved fluvial erosion, although the style of this erosion (such as surface runoff, groundwater discharge, or sapping) remains controversial. Valley network systems are confined mainly to the southern highlands on Noachian terrain and display variability in the number of tributaries, stream order, and planimetric form (*21*). Additionally, nearly all martian outflow channels (*20*) originate in or flow into the Tharsis trough (Fig. 3A).

We tested for control of valley network orientations by Tharsis loading. Gradient directions of both modeled [augmented with the pole-to-pole slope (*5*)] and observed topography were calculated at the downstream ends of valley network trunks. The level of agreement of topographic gradients with valley network downstream azimuths (*22*) was evaluated by forming the dot products, cos δ, of unit directional vector pairs (*23*). Histograms of cos δ distributions for the modeled (Fig. 4A) and observed (Fig. 4B) topography ($l = 10$) support significant Tharsis influence on long-wavelength topography and valley network azimuths. Because of the multiscale morphology of valley network systems, any assessment of azimuth will depend on baseline length. Our estimates of azimuth are based on the long-baseline orientation of the trunk valley. As such, they are most sensitive to slopes with length scales comparable to the size of the basin drained by the valley network system, and not to slopes with shorter length scales (*24*). For only a subset (~60%) of valley network systems—where local topography is not dominated by short length scales—do we find that valley network azimuths agree with the gradient directions of the observed topography. Thus, it is appropriate to consider the relative success of modeled topography as compared to observed topography in predicting valley network azimuths. Using the two histogram modes ($0.8 \leq \cos\delta \leq 1.0$), the model-to-topography ratio is 100% for an expansion limit of $l = 10$ (~1000 km minimum length scale) and exceeds 70% at $l = 180$ (~50 km minimum length scale) (Fig. 4C). We conclude that the model (Fig. 4D) does a satisfactory job of

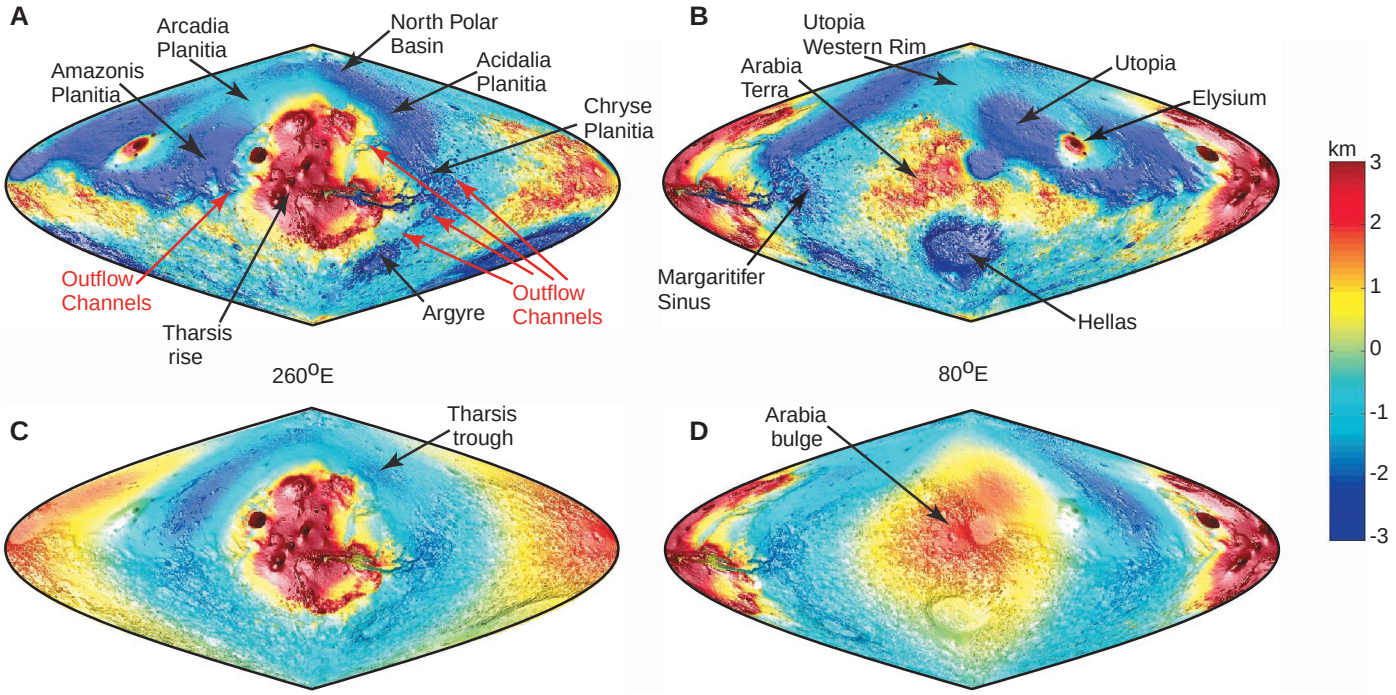

Fig. 3. Observed martian topography displayed for (**A**) the Tharsis and (**B**) the anti-Tharsis hemispheres compared with modeled topography (to $l = 120$) for (**C**) the Tharsis and (**D**) the anti-Tharsis hemispheres. For the model, actual topography is shown in the Tharsis region. All figures are draped over a 3D view of shaded relief.

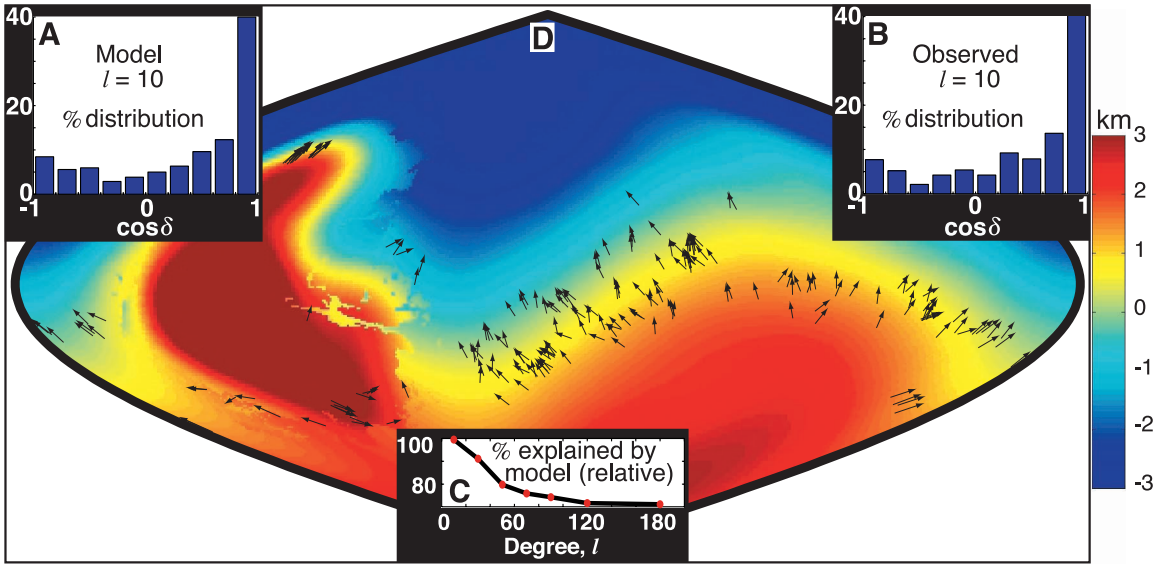

Fig. 4. (**A**) Histogram of cos δ [dot product of model gradient (l = 10) and valley network azimuth unit vectors] distribution. (**B**) Histogram as in (A), but for observed topography. The P value for the null hypothesis of a uniform distribution is less than 10^{-16} for both histograms. (**C**) The model-to-topography ratio (%) for the modes of the histograms as a function of spherical harmonic expansion limit l. (**D**) Black arrows correspond to valley networks in (A) for cos δ ≥ 0.8. The background color image is the model response to Tharsis loading (l = 10) that has been saturated at ±3 km. Central longitude is 0°, and observed topography is shown in the Tharsis region. Pole-to-pole slope has been included in the topographic model, which has been referenced to the observed geoid.

explaining valley network azimuths and that many of these systems must have formed after a significant fraction of the Tharsis load was in place.

Valley networks were examined in detail (*25*) in Margaritifer Sinus, a region on the flank of the Arabia bulge and in the Tharsis trough (Fig. 3B). Most formed on regions of relatively high topographic gradient on the flanks of the trough. The majority (~85%) of observed valley networks here likely formed in Late Noachian time, between ~4.3 to 3.85 billion years ago (Ga) and ~3.8 to 3.50 Ga (*26*), although the possibility exists that earlier valley networks in this region were destroyed by a high impact flux or alternative erosion mechanisms. Because many of these valley network orientations are controlled by Tharsis-induced slopes, the Tharsis load must be largely Noachian in age, which is consistent with inferences made earlier. Superposition and sequence relationships indicate that the valley networks whose azimuths are not explained by the model are nevertheless contemporaneous with the Tharsis-controlled valley networks (*27*). The formation of valley networks in Margaritifer Sinus is intimately associated with a Late Noachian, large-scale erosion event on the flanks of the Tharsis trough that stripped at least 1.5×10^6 km^3 of material from this area, leaving behind numerous mesas of Early and Middle Noachian terrain (*25*). This same process may have operated in adjacent areas of northwestern Arabia Terra, potentially removing an additional 3×10^6 km^3 of the upper crust. Moreover, a global episode of high erosion rates at the end of the Noachian Epoch has been postulated on the basis of crater size-frequency statistics and morphology (*28*). Thus, there is evidence that the Late Noachian was a time of unusually high landscape modification rates on Mars. The most likely erosional agent is water at or near the surface, which is consistent with a warmer, wetter environment than at present (*29*).

The release of CO_2 and H_2O to the martian atmosphere from magma erupted and intruded during Tharsis formation may have affected the Noachian climate. For the 100-km-thick elastic lithosphere we assume (*2*), the observed topography plus the volume of material contained within the depression resulting from Tharsis loading amounts to $\sim 3 \times 10^8$ km^3 of igneous material, which is equivalent to a 2-km-thick global layer (*30*). For a magmatic CO_2 content of 0.65 weight percent (wt %) [which is consistent with Hawaiian basaltic lavas (*31*)] and an H_2O content of 2 wt % (*32*), the total release of gases from Tharsis magmas could produce the integrated equivalent of a 1.5-bar CO_2 atmosphere and a 120-m-thick global layer of water. These quantities of volatiles are sufficient to warm the atmosphere to the point at which liquid water is stable at the surface (*33*). The accumulation of atmospheric CO_2 may have made the latter part of the Noachian the most favorable time for this condition.

As the emplacement rate of Tharsis volcanic material declined at the end of the Noachian, CO_2 and H_2O would have been removed from the atmosphere by a combination of impact ejection to space, stripping by the solar wind, thermal escape, and the formation of carbonate minerals on the surface or within the crust (*34*, *35*). Although their relative importance cannot be determined, there is evidence that each of these processes has occurred, and it is possible that, combined, they could have brought clement conditions to an end by removing substantial quantities of atmosphere in less than a few hundred million years (*35*). With several events occurring at the end of the Noachian, such as the decline in impact rate, initiation of sputtering as the internal magnetic field disappears (*35*), waning of Tharsis volcanism, and a decrease in surface erosion rate, it is difficult to determine which were causally related and which were coincidental. Nevertheless, it is possible that during the Noachian Epoch, the structural and magmatic events associated with Tharsis evolution were the sine qua non that linked fluvial, geodynamical, and climate activity.

References and Notes

1. S. C. Solomon, J. W. Head, *J. Geophys. Res.* **87**, 9755 (1982).
2. M. T. Zuber *et al.*, *Science* **287**, 1788 (2000).
3. W. B. Banerdt, M. P. Golombek, K. L. Tanaka, in *Mars*, H. H. Kieffer, B. M. Jakosky, C. W. Snyder, M. S. Matthews, Eds. (Univ. of Arizona Press, Tucson, AZ, 1992), pp. 249–297.
4. D. E. Smith *et al.*, *Science* **286**, 94 (1999).
5. D. E. Smith *et al.*, *Science* **284**, 1495 (1999).
6. A. L. Albee, F. D. Palluconi, R. E. Arvidson, *Science* **279**, 1671 (1998).
7. In Figs. 1, 2B, 2C, and 3, the observed pole-to-pole topographic slope (*5*) has been removed in order to focus the dynamic range of the color scales and shaded relief perspectives on regional variations of observed or modeled topography.
8. W. B. Banerdt, *J. Geophys. Res.* **91**, 403 (1986).
9. We assumed the following conditions: elastic shell thickness = 100 km, Young's modulus = 100 GPa, Poisson's ratio = 0.25, and crustal thickness = 50 km (*2*).
10. In the absence of precise topographic information, this approach was first used with an analytic approximation of load geometry [R. J. Willemann, D. L. Turcotte, *J. Geophys. Res.* **87**, 9793 (1982)]. We zeroed topography outside of Tharsis, using, for computational convenience, the zero elevation contour on a quarter-degree grid of topography. To obtain spherical harmonic coefficients for the load, we expanded the isolated Tharsis topography to degree and order 120 (l = 120) to minimize ringing from

the truncated topography [M. T. Zuber, D. E. Smith, *J. Geophys. Res.* **102**, 28673 (1997)]. In our approach and in earlier approaches that did not isolate the Tharsis load, the total load acting on the lithosphere consists of the topographic load plus the load necessary to account for the deformational response of the lithosphere to the imposed topographic load. Beneath Tharsis, the deformation is a depression.
11. This 95% compensation figure is an average over wavelengths corresponding to spherical harmonic degrees $l \leq 10$.
12. W. M. Folkner, C. F. Yoder, D. N. Yuan, E. M. Standish, R. A. Preston, *Science* **278**, 1749 (1997).
13. The gravity mismatch could be remedied by introducing a degree of isostatic compensation into the topography induced by the Tharsis load (*8*). Nonetheless, spatial patterns of predicted gravity anomalies and topography and how well they correlate with patterns in the observed fields are valid with the present model because the planet responds to the load only at very long wavelengths ($l \leq 10$). [D. L. Turcotte, R. J. Willemann, W. F. Haxby, J. Norberry, *J. Geophys. Res.* **86**, 3951 (1981)]. At such wavelengths, the load is supported by the resistance of the elastic shell to changes in its radius of curvature. This resistance is known as a "membrane stress." Because of membrane stress load support, plausible variations in the thickness and elastic properties of the lithospheric shell do not affect the spatial patterns of the modeled anomalies.
14. The trough may have been obscured by later deformation, evidence for which includes a series of ridges concentric to the Tharsis rise (*5*) [R. A. Schultz, K. L. Tanaka, *J. Geophys. Res.* **99**, 8371 (1994)], and by early volcanic and sedimentary deposition at the edges of the Tharsis rise (*15*).
15. D. H. Scott, K. L. Tanaka, *U.S. Geological Survey Map I-1802-A* (1986).
16. On the basis of impact crater counts, Mars has been divided into three main epochs of time; from oldest to youngest, they are the Noachian, Hesperian, and Amazonian. Assignment of absolute ages to the epoch boundaries is dependent on models for the impact flux rate. Two specific models place the Noachian-Hesperian boundary at 3.8 and 3.5 Ga and the Hesperian-Amazonian boundary at 3.55 and 1.8 Ga (*26*).
17. R. C. Anderson *et al.*, *J. Geophys. Res.*, in press.
18. Recent modeling [W. B. Banerdt, M. P. Golombek, *Lunar Planet. Sci.* **31**, abstr. 2038 (2000)] using gravity and topography fields derived from MGS observations, which are of higher degree and order than were available before, indicates that load support by bending and membrane stresses can explain the type, location, orientation, and strain of the majority of Tharsis structural features.
19. Early tectonic activity substantially predates many of the surface units of Tharsis (*15*), which typically are comparatively thin Hesperian and Amazonian deposits covering the earlier Noachian units [J. B. Plescia, R. S. Saunders, *Proc. Lunar Planet. Sci. Conf.* **11**, 2423 (1980)].
20. M. H. Carr, *Water on Mars* (Oxford Univ. Press, New York, 1996).
21. ———, *J. Geophys. Res.* **100**, 7479 (1995).
22. Azimuths were estimated from a database (*21*) consisting of almost 8000 branch segments composing over 800 valley network systems located between 47.5°N and 47.5°S. The number of valley network systems used here was reduced to 520 by eliminating systems whose downstream directions are ambiguous and by excluding valley networks that flow into the Hellas impact basin, inasmuch as their directions cannot be predicted by the model.
23. The distribution of cos δ lies between –1 and 1, with 1 meaning perfect agreement in orientation and –1 meaning that the vectors have exactly the opposite directions.
24. K. Chan, D. H. Rothman, *Phys. Rev. E*, in press.
25. B. M. Hynek, R. J. Phillips, *Geology*, in press.
26. K. L. Tanaka, D. H. Scott, R. Greeley, in *Mars*, H. H. Kieffer, B. M. Jakosky, C. W. Snyder, M. S. Matthews, Eds. (Univ. of Arizona Press, Tucson, AZ, 1992), pp. 345–382.
27. Mapped valley networks within Margaritifer Sinus (*15*, *25*) that do not have azimuths explained by the model occur almost exclusively on the same mapped unit as those that fit the model, and hence are likely to be contemporaneous. Also indicative of an equivalent age is the observation that crater densities are, within error, identical on the terrains containing network azimuths that follow and do not follow long-wavelength topography (*25*).
28. C. R. Chapman, K. L. Jones, *Annu. Rev. Earth Planet. Sci.* **5**, 515 (1977).
29. R. A. Craddock, T. A. Maxwell, *J. Geophys. Res.* **98**, 3453 (1993).
30. Horizontal layering to thicknesses of at least 8 km has been observed in the canyon walls of Valles Marineris and has been interpreted as volcanic in origin and mostly Noachian in age [A. S. McEwen, M. C. Malin, M. H. Carr, W. K. Hartmann, *Nature* **397**, 584 (1999)]. From this observation, the volcanic volume in the Valles Marineris region is estimated at $\sim 4 \times 10^7$ km^3. Because this is only a small areal fraction on a flank of the Tharsis rise, the total volume of magmatic material associated with Tharsis overall must be approximately an order of magnitude larger, which is consistent with our model results.
31. T. M. Gerlach, E. J. Graber, *Nature* **313**, 273 (1985).
32. H. Y. McSween Jr. *et al.*, *Nature* **409**, 487 (2001).
33. F. Forget, R. T. Pierrehumbert, *Science* **278**, 1273 (1997).
34. D. A. Brain, B. M. Jakosky, *J. Geophys. Res.* **103**, 22 (1998).
35. M. H. Carr, *J. Geophys. Res.* **104**, 21 (1999).
36. We thank the MGS Radio Science and the Mars Orbiter Laser Altimeter (MOLA) investigations, which are supported by the NASA Mars Exploration Program.

29 December 2000; accepted 2 March 2001
Published online 15 March 2001;
10.1126/science.1058701
Include this information when citing this paper.

Role of the Stratospheric Polar Freezing Belt in Denitrification

A. Tabazadeh,[1]* E. J. Jensen,[1] O. B. Toon,[2] K. Drdla,[1] M. R. Schoeberl[3]

Homogeneous freezing of nitric acid hydrate particles can produce a polar freezing belt in either hemisphere that can cause denitrification. Computed denitrification profiles for one Antarctic and two Arctic cold winters are presented. The vertical range over which denitrification occurs is normally quite deep in the Antarctic but limited in the Arctic. A 4 kelvin decrease in the temperature of the Arctic stratosphere due to anthropogenic and/or natural effects can trigger the occurrence of widespread severe denitrification. Ozone loss is amplified in a denitrified stratosphere, so the effects of falling temperatures in promoting denitrification must be considered in assessment studies of ozone recovery trends.

Polar stratospheric cloud (PSC) sightings date back to the 19th century (*1*). Up to a few decades ago, PSCs were known primarily for their colorful glows that occasionally filled up the skies over the poles in winter and early spring. Soon after the discovery of the springtime Antarctic "ozone hole" (*2*), chlorofluorocarbons (CFCs) (*3*) along with naturally occurring PSCs (*4*) were identified as important agents in ozone destruction. It was hypothesized (*4*) and later proven (*5*, *6*) that PSCs promote formation of active chlorine, originally derived from man-made emission of CFCs (*3*), that catalytically destroys ozone molecules.

Another interesting feature of some PSCs is that they contain large amounts of nitric acid (*7*, *8*). Recent analysis of space-borne observations (*9*) indicates that a continuous downward flow of large cloud particles (larger than a few micrometers) can form within persistent PSCs. This flux of large particles can remove a substantial amount of nitric acid from the altitude range in which PSCs can form (~16 to 24 km) in periods of less than 2 weeks (*9*). The process of irreversible nitric acid removal from the stratosphere is known as denitrification (*7*, *10*, *11*). Currently, it occurs extensively only inside the Antarctic vortex (*9*, *12*). A denitrified stratosphere in early spring is primed for ozone destruction because reactive nitrogen that can mediate ozone loss (by sequestering active chlorine) has been removed from the stratosphere (*13*).

Even after more than a decade of research on PSCs, a quantitative understanding of how large nitric acid–containing cloud particles (*14*) form in the stratosphere has remained elusive (*13*, *15*). Many in situ and remote sensing observations show the existence of both small liquid and large solid cloud particles containing nitric acid in the polar stratosphere (*13*, *16*). Liquid nitric acid–containing cloud particles are composed of supercooled ternary solutions (STS) of nitric acid, sulfuric acid, and water (*17*, *18*). Because STS particles form by condensational growth, their

[1]NASA Ames Research Center, Earth Science Division, MS:245-4 Moffett Field, CA 94035, USA. [2]Laboratory for Atmospheric and Space Physics, Program in Atmospheric and Oceanic Sciences, University of Colorado, Boulder, CO 80309, USA. [3]NASA Goddard Space Flight Center, Greenbelt, MD 20771, USA.

*To whom correspondence should be addressed. E-mail: atabazadeh@mail.arc.nasa.gov